TG-43 Characterization of the IPL 67-6500 ^{137}Cs Tube Source using Monte Carlo Transport Calculations

Final Report

Tim D. Bohm

Larry A. DeWerd

May 20, 2004

Department of Medical Physics

University of Wisconsin-Madison

1 Introduction

The purpose of this document is to provide a final report on research work performed for TG-43 characterization of the IPL 67-6500 ^{137}Cs tube source using Monte Carlo transport calculations. Use of Monte Carlo transport calculations is a common and accepted method to determine TG-43 dosimetry parameters for brachytherapy sources [1, 2].

2 Materials and Methods

2.1 Tube Source

The IPL model 67-6500 ^{137}Cs source is a cylindrically shaped stainless steel tube source. It has an overall length of 2 cm with a diameter of 0.3 cm. The active region is a ceramic cylinder 1.48 cm long and 0.15 cm in diameter. The active region is encapsulated with two stainless steel walls with a total thickness of 0.0584 cm. For the purposes of this report, the origin is taken at the active region center with the swage plug end of the source corresponding to $\theta = 180^o$.

2.2 Monte Carlo code and library description

MCNP is a Monte Carlo transport code system developed at Los Alamos National Laboratory [3]. MCNP is a generalized, continuous energy, three dimensional coupled neutron/photon/electron Monte Carlo transport code. MCNP traditionally uses a surface-sense geometry method where intersections and unions of first degree, second degree, and some fourth degree surfaces are used to define the problem geometry. Recently, a macrobody capability has been added to give MCNP a combinatorial geometry capability. MCNP's geometry package is user friendly and allows complicated geometric models to be developed easily.

The calculations in this work were performed using MCNP version 4c3. The detailed photon physics option of MCNP was used in this work and includes treatment of coherent scattering, incoherent (Compton) scattering, photoelectric effect (with K and L shell fluo-

rescence and Auger electron production following atomic relaxation) and pair production. Because the photoelectric cross sections for low Z materials used by some MCNP photon libraries are somewhat out of date, the fully updated library, *mcplib04* [4], was used. This library contains updated cross sections, form factors, scattering functions, and fluorescence data. The library is based on ENDF/B-VI release 8 whose cross sections are based on Lawrence Livermore National Laboratories EPDL-97 [5].

The electron transport method implemented in MCNP is a class I condensed history method with physics at the level of the Integrated Tiger Series (ITS) version 3 [3, 6]. In MCNP, the condensed random walk for electron transport is based on energy steps (major steps). Pre-calculated and tabulated data for the electrons are saved on a predefined energy grid which corresponds to an average energy loss of 8.3% per major step [3]. The electron trajectory and production of secondary particles are controlled at the substep level. MCNP, like the ETRAN and ITS codes, uses the Goudsmit-Saunderson multiple scattering distribution to treat the angular deflection of the electron during its sub-step. MCNP and its associated cross section libraries can treat photon and electron transport down to 1 keV.

2.3 Calculation description

A detailed model of the IPL tube source was developed based on engineering drawings and material specifications from the manufacturer. Note that differences in the "as-built" dimensions can significantly change the source output dosimetry from that of the engineering model. These issues are not addressed in this work and it is recommended that sources be imaged to reveal any differences between engineering models and "as-built" dimensions [11]. Figure 1 shows the model developed for MCNP. Figure 1(b) shows a close up view of the top portion of the tube source with the swage plug and aluminum ring. A cut-out view is used to show the source interior.

The photon spectrum for ^{137}Cs was taken from the Table of Radioactive Isotopes [7] . The mean photon energy for this spectrum is 613 keV, however the spectrum is dominated by a 662 keV gamma ray. The beta spectrum for ^{137}Cs was taken from ICRU-56 [8]. The mean beta energy for this spectrum is 168 keV with a maximum endpoint energy of 1176

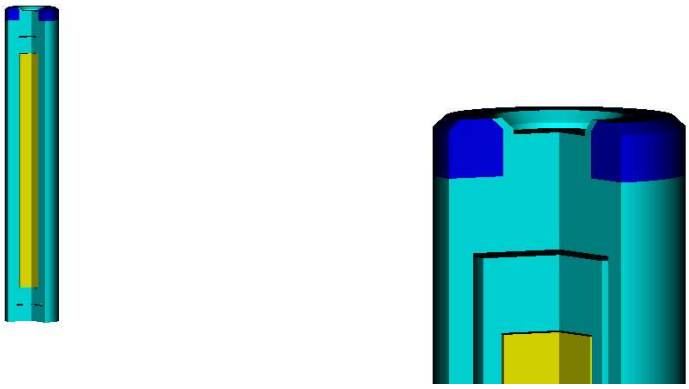

(a) Overall view. (b) Upper portion view.

Figure 1: The IPL model 67-6500 tube source as modeled with MCNP. A cut-out view is shown to reveal the interior.

keV.

Material compositions for air and water were taken from the updated TG-43 recommendations [2].

3 Results

3.1 Cross section comparison

Because the cross section libraries are the most fundamental component of a transport calculation, the cross section library used with MCNP (*mcplib04*) was compared to the XCOM cross sections available from NIST [9]. Figure 2, Figure 3, and Figure 4 show the photon macroscopic cross sections (attenuation coefficients) from *mcplib04* and XCOM for ceramic, stainless steel 304, and water over the photon energies of interest for this work. In general the agreement is quite good. Notice that the MCNP library is tabulated on a much finer energy grid than the NIST data. This allows for a more detailed representation of the cross section behavior and smaller interpolation errors when performing continuous energy particle transport.

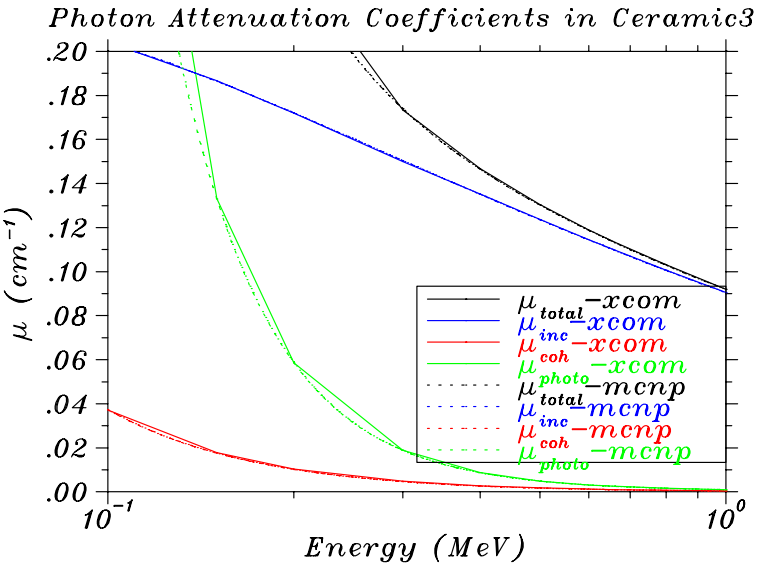

Figure 2: Comparison of *mcplib04* and XCOM photon cross sections in ceramic.

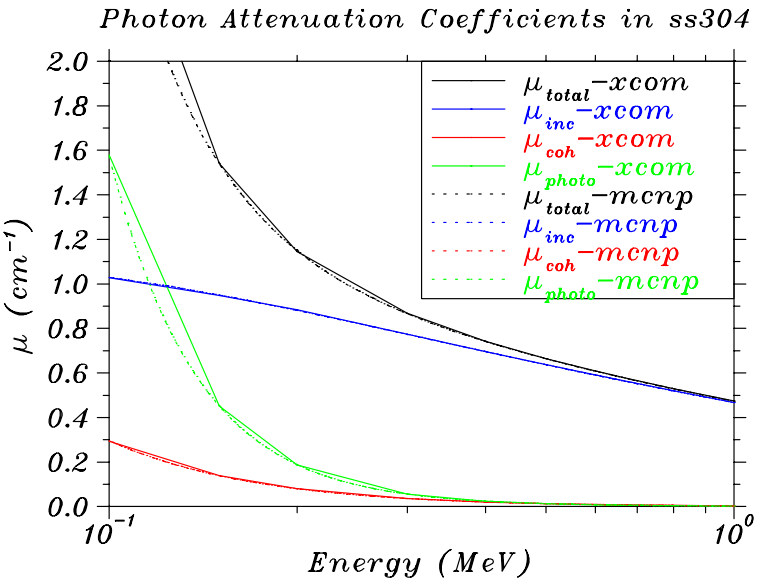

Figure 3: Comparison of *mcplib04* and XCOM photon cross sections in Stainless Steel 304.

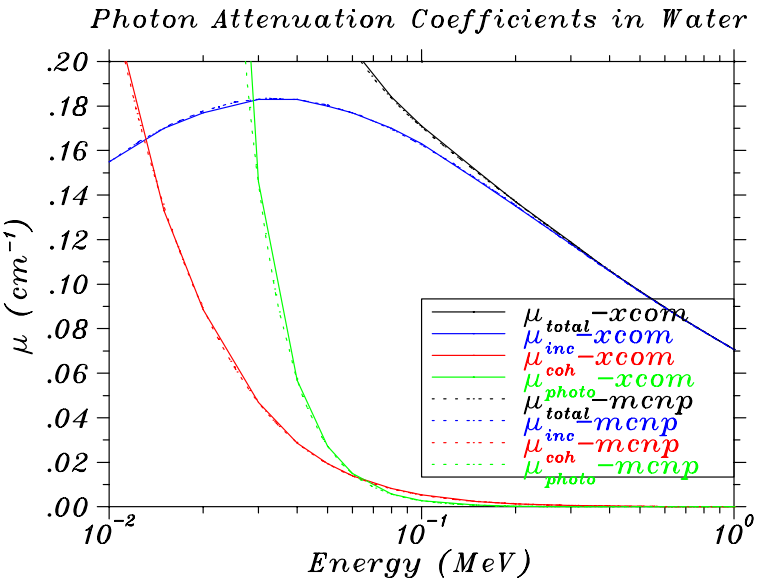

Figure 4: Comparison of *mcplib04* and XCOM photon cross sections in water.

3.2 Depth-Dose in water/Radial dose function $g(r)$

Because ^{137}Cs emits both betas and photons during decay [7], the total dose in water is the dose in water due to the beta emission plus the dose in water due the photon emission.

3.2.1 β Component

^{137}Cs emits betas with a maximum energy of 1175.63 keV [7] and betas of this energy may penetrate the stainless steel encapsulation. Figure 5 shows the beta spectrum for ^{137}Cs taken from ICRU 56 [8]. The average beta energy for this distribution is 0.168 MeV which is too low to penetrate the encapsulation. However, these betas produce bremsstrahlung and atomic relaxation photons while slowing down in the ceramic and stainless steel encapsulation which can penetrate the encapsulation. Figure 6 shows the photon spectrum leaving the tube encapsulation from the beta emission of ^{137}Cs. Approximately 0.25 photons per 100 betas emitted leave the source encapsulation. This is a small number and we expect that it will not contribute substantially to the total dose in water.

At 1 cm depth in water, the beta emission component of total dose in water is over 1000 times smaller than the photon emission component. Therefore, only the photon component

of total dose to water will be reported.

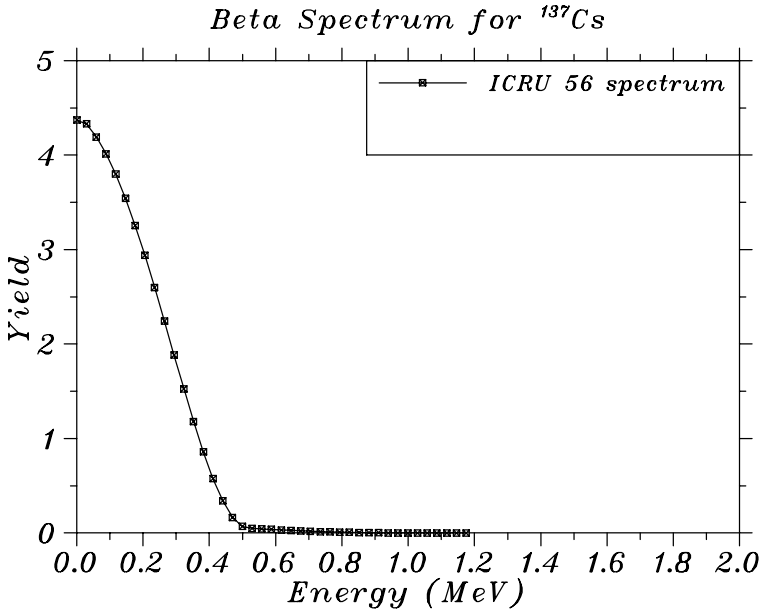

Figure 5: ^{137}Cs beta spectrum from ICRU 56 [8].

3.2.2 Photon Component

The depth dose in water was determined with calculations of MCNP using four different tally types over depths of 0-10 cm. The tally types *f4, *f5, f6, and *f8 were used. Tally types *f4 and f6 are track length estimators while tally type *f5 is a modified next event estimator. Tally type *f8 is a cell energy balance estimator. The *f4 and *f5 tallies used energy absorption coefficients from Hubbell and Seltzer [10] while the f6 tally uses MCNP's energy absorption coefficients. All of these tallies produced similar results for depth dose values with the largest average differences between tallies of 0.56%.

Because these tallies produced very similar results and because treatment of fully coupled photon-electron transport is very computationally expensive, the next event estimator tallies will be used for determining dose in water for this work. This is consistent with the method used in the work of Williamson [11]. The next event estimator also has the advantage of not introducing volume averaging effects since it is not a track length estimator. For the depth dose in water calculations necessary to determine the radial dose function, the statistical

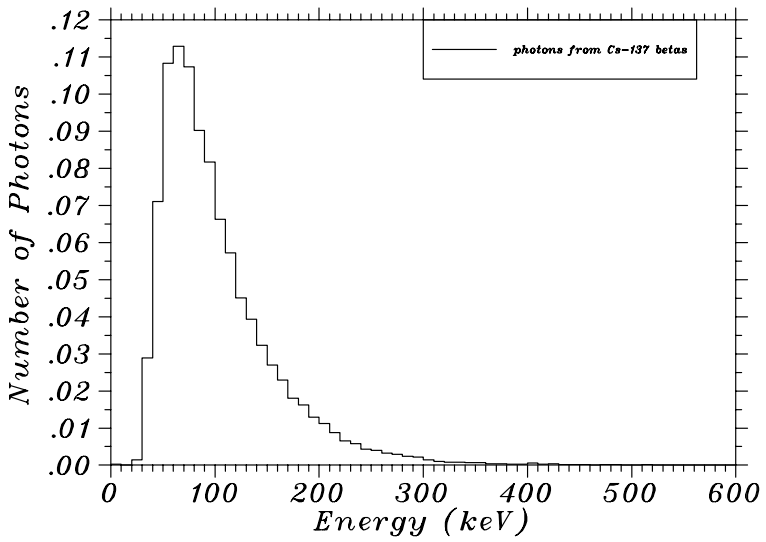

Figure 6: Photon spectrum escaping IPL tube encapsulation from ^{137}Cs β emission.

uncertainty averaged less than 0.1%.

Table 1 shows the radial dose function for the IPL 67-6500 tube source as determined with MCNP. The line source approximation with an active source length L=1.48 cm was used for determining the geometry factor for the IPL source. For the depth dose data needed to determine the radial dose function shown in this table, the *mcplib04* energy absorption coefficients were used with the next event estimator tally. Use of Hubbell and Seltzer energy absorption coefficients to determine the radial dose function produced differences less than 0.35%.

For comparison, the radial dose function data is shown with the data from Casal *et al.* [12] for the Amersham CDCS-M source in Figure 7(a). Casal *et al.* used the Monte Carlo code GEANT to determine the radial dose function. Agreement between this work and Casal *et al.* is good with a maximum percent difference of 0.49% over 0.25-15 cm depth in water.

For further comparison, the data from Liu *et al.* [13] is also shown in Figure 7(b). Note that the data from Liu is an average over several seed designs and is calculated with the Sievert Integral method. Liu *et al.* had seen little differences in the radial dose function for the sources investigated in their work. Agreement between this work and Liu *et al.* is good with an average percent difference of 0.3% and maximum percent difference of 1.6% over

0.5-10. cm depth in water.

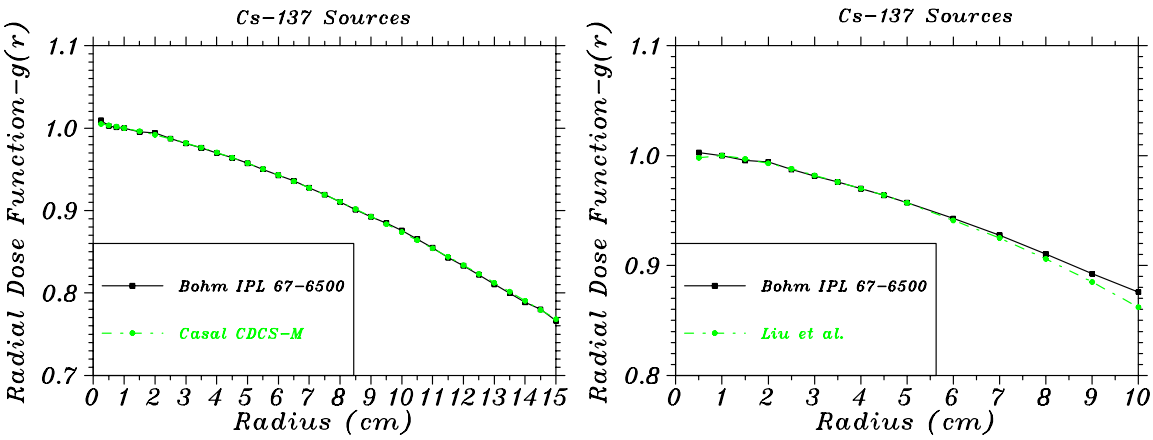

(a) IPL 67-6500 tube source versus Amersham CDCS-M.

(b) IPL 67-6500 tube source versus Liu *et al.'s* average of ^{137}Cs tube sources.

Figure 7: Comparison of g(r) for IPL 67-6500 tube source versus Casal *et al.* [12] and Liu *et al.* [13].

Additionally, comparisons were made with the data from Williamson [11] and are shown in Figure 8(a) for the Amersham CDCS-J type source. Williamson used his PTRAN Monte Carlo transport code with the DLC-99 cross section library to determine the dosimetry for the Amersham source. Agreement between this work and Williamson is good with an average percent difference of 0.6% and maximum percent difference of 1.9% over 0.25-7. cm depth in water. Figure 8(b) compares the radial dose function for the IPL 67-6500 tube source versus the 3M 6500 source. Again, agreement is good with with an average percent difference of 0.6% and maximum percent difference of 1.9% over 0.25-7. cm depth in water.

In general, the radial dose function determined in this work for the IPL source is in good agreement with that of other published work for different cesium tube sources. The small differences seen at depths in water may be due to differences in source design including variations in source geometry, active materials, and encapsulation dimensions. Additionally, differences between this work and Williamson's work may be due to the use of different cross section libraries. Note that MCNP's *mcplib04* cross section library is a more recent

Table 1: Radial dose function as determined with MCNP for the IPL 67-6500 ^{137}Cs tube source.

Depth (cm)	$g(r)$
0.25	1.009
0.50	1.003
0.75	1.001
1.00	1.000
1.50	0.995
2.00	0.994
2.50	0.987
3.00	0.981
3.50	0.976
4.00	0.970
4.50	0.964
5.00	0.957
5.50	0.950
6.00	0.943
6.50	0.936
7.00	0.928
7.50	0.919
8.00	0.910
8.50	0.901
9.00	0.892
9.50	0.885
10.00	0.876
10.50	0.865
11.00	0.855
11.50	0.843
12.00	0.833
12.50	0.822
13.00	0.810
13.50	0.800
14.00	0.789
14.50	0.780
15.00	0.766

evaluation of photon data than the DLC-99 library used by Williamson.

For further comparison, the depth dose in water was calculated with MCNP5 which has a small improvement in its treatment of incoherent scattering [17]. The MCNP4c3 results presented in this work were in good agreement with the MCNP5 results. The average difference in dose was 0.1% with a maximum difference in dose of 0.27% observed over a 0.25cm to 15 cm depth in water for the IPL 67-6500 tube source.

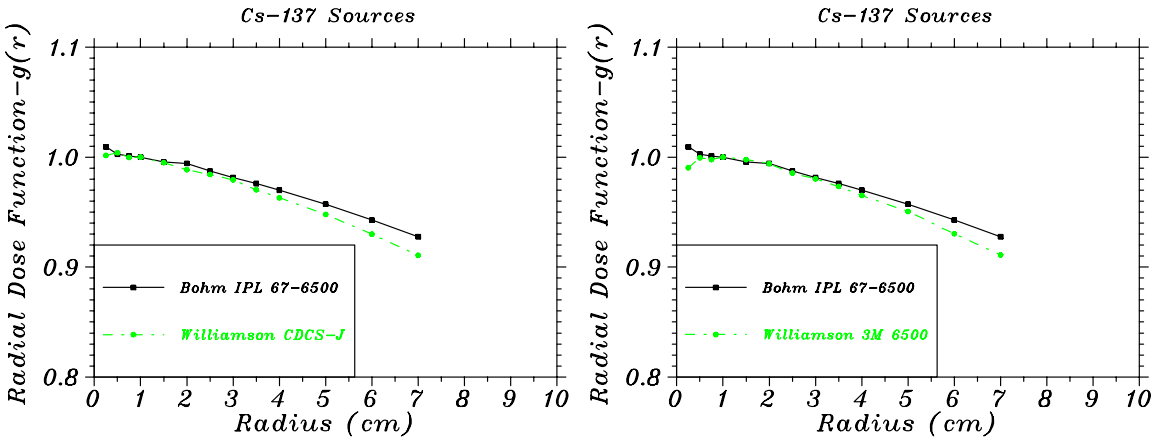

(a) IPL 67-6500 tube source versus Amersham CDCS-J source.

(b) IPL 67-6500 tube source versus 3M 6500 source.

Figure 8: Comparison of g(r) for IPL 67-6500 tube source versus Williamson [11].

4 2D Anisotropy Function $F(r, \theta)$

Table 2 shows the 2D Anisotropy function for the IPL 67-6500 tube source as determined with MCNP. The line source approximation with an active source length of L=1.48 cm was used for determining the geometry factor for the IPL source. Note that for this work, the origin is centered in the active region of the source and the swage plug end of the source corresponds to $\theta = 180^o$. For the results presented in table 2, the *mcplib04* energy absorption coefficients were used with the next event estimator tally. Little or no difference was observed when using the Hubbell and Seltzer energy absorption coefficients. For the depth dose in

water calculations necessary to determine the anisotropy function, the statistical uncertainty averaged less than 0.25%.

For comparison, the anisotropy function at r=2 cm is plotted versus that obtained by Casal *et al.* [12] in Figure 9. Agreement near the transverse axis is good with the largest differences seen at points near the source axis. This is expected since the two sources have different encapsulations at the ends. For example, at the $\theta = 0^o$ position, the CDCS-M source has 0.31 cm encapsulation while the IPL source has .20 cm of encapsulation. For

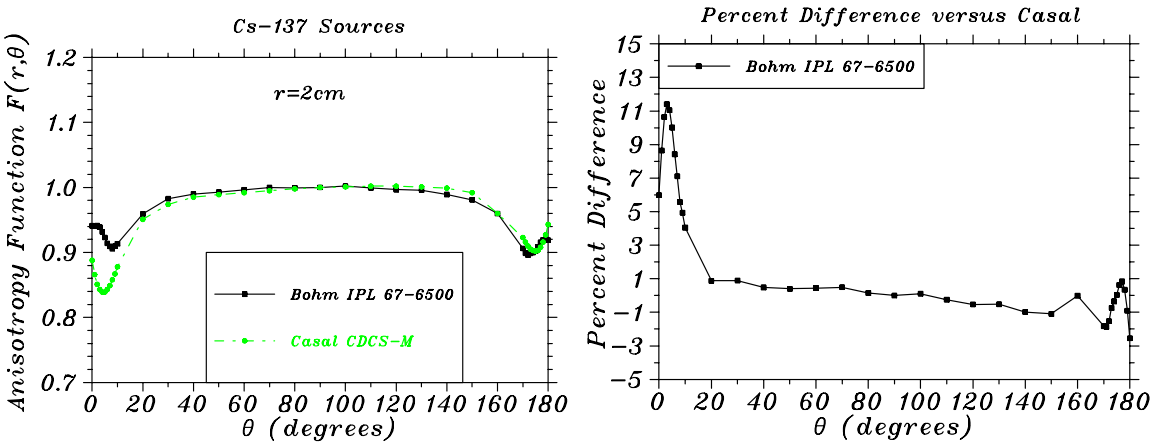

(a) $F(r = 2cm, \theta)$.

(b) Percent difference in $F(r = 2cm, \theta)$.

Figure 9: Anisotropy function profile at r=2cm for for IPL 67-6500 tube source versus Casal *et al.* for CDCS-M source.

further comparison, the anisotropy function at r=2 cm is plotted versus that obtained by Liu [13] in Figure 10. Agreement near the transverse axis is good with the largest differences seen at points near the source ends. Liu report anisotropy functions determined using the Sievert Integral method averaged over several ^{137}Cs sources.

In order to illustrate the sensitivity of the anisotropy function, the encapsulation at the bottom end of the IPL source was reduced from .2032 cm to .1016 cm of stainless steel. Figure 11 shows the resulting anisotropy function at r=1.5cm. Note the increase in the anisotropy function near $\theta = 0^o$.

Table 2: 2D Anisotropy function as determined with MCNP for the IPL 67-6500 ^{137}Cs tube source. Note that for this work, the origin is centered in the active region of the source and the swage plug end of the source corresponds to $\theta = 180^o$.

θ (deg)	r (cm)														
	0.25	0.50	0.75	1.00	1.25	1.50	2.00	3.00	4.00	5.00	6.00	7.00	8.00	10.00	15.00
0.	*****	*****	*****	0.950	0.946	0.945	0.941	0.938	0.937	0.939	0.935	0.937	0.934	0.946	0.943
1.	*****	*****	*****	0.952	0.946	0.944	0.941	0.936	0.935	0.938	0.934	0.936	0.937	0.952	0.943
2.	*****	*****	*****	0.953	0.946	0.944	0.942	0.938	0.940	0.938	0.930	0.930	0.934	0.940	0.933
3.	*****	*****	*****	0.952	0.946	0.943	0.939	0.930	0.925	0.925	0.919	0.919	0.921	0.932	0.929
4.	*****	*****	*****	0.953	0.946	0.942	0.932	0.923	0.924	0.924	0.918	0.919	0.924	0.930	0.936
5.	*****	*****	*****	0.953	0.940	0.932	0.923	0.915	0.913	0.916	0.911	0.913	0.917	0.925	0.926
6.	*****	*****	*****	0.947	0.929	0.923	0.914	0.907	0.923	0.915	0.911	0.911	0.916	0.927	0.932
7.	*****	*****	*****	0.934	0.924	0.918	0.909	0.904	0.905	0.909	0.906	0.908	0.919	0.925	0.936
8.	*****	*****	*****	0.931	0.917	0.910	0.906	0.905	0.909	0.913	0.909	0.912	0.919	0.924	0.935
9.	*****	*****	*****	0.925	0.915	0.914	0.910	0.908	0.910	0.914	0.912	0.915	0.920	0.928	0.934
10.	*****	*****	*****	0.931	0.918	0.916	0.914	0.913	0.916	0.919	0.916	0.921	0.924	0.933	0.945
20.	*****	1.023	1.003	0.979	0.969	0.964	0.959	0.957	0.956	0.957	0.956	0.969	0.958	0.962	0.964
30.	*****	1.010	1.002	0.992	0.985	0.985	0.983	0.978	0.978	0.980	0.977	0.976	0.976	0.981	0.982
40.	1.018	1.002	0.998	0.995	0.992	0.991	0.990	0.989	0.987	0.989	0.987	0.987	0.988	0.988	0.988
50.	1.009	1.002	1.005	0.997	0.995	0.994	0.993	0.993	0.993	0.993	0.992	0.992	0.994	0.995	1.004
60.	1.005	1.000	0.999	0.997	0.999	0.999	0.996	0.996	0.995	0.997	0.994	0.995	0.995	0.996	0.997
70.	1.003	1.000	0.998	0.999	0.998	1.002	1.000	0.999	0.998	1.001	0.996	0.998	0.998	1.005	0.999
80.	1.001	1.003	0.999	0.998	0.998	0.999	1.000	0.999	0.998	1.000	0.997	0.998	1.002	0.999	1.000
90.	1.000	1.000	1.000	1.000	1.000	1.000	1.000	1.000	1.000	1.000	1.000	1.000	1.000	1.000	1.000
100.	1.001	1.001	1.004	0.999	0.999	1.000	1.002	1.000	1.001	1.001	1.007	1.001	1.001	1.000	1.005
110.	1.004	1.002	1.000	0.999	0.999	1.000	1.000	1.000	0.999	1.000	0.995	0.996	0.997	1.001	1.000
120.	1.003	1.000	0.998	0.998	0.996	0.996	0.997	0.996	0.995	0.997	0.996	0.994	0.996	0.998	0.996
130.	1.009	1.002	0.999	0.997	0.996	0.998	0.996	0.995	0.993	0.995	0.993	0.994	0.994	0.996	0.996
140.	1.019	1.005	0.999	0.994	0.992	0.991	0.989	0.990	0.988	0.988	0.985	0.987	0.987	0.987	0.984
150.	*****	1.011	1.001	0.991	0.986	0.984	0.981	0.981	0.979	0.979	0.977	0.976	0.975	0.983	0.979
160.	*****	1.027	1.003	0.978	0.968	0.965	0.960	0.957	0.956	0.956	0.955	0.955	0.958	0.959	0.971
170.	*****	*****	*****	0.933	0.914	0.908	0.906	0.907	0.910	0.913	0.915	0.919	0.923	0.930	0.933
171.	*****	*****	*****	*****	0.906	0.901	0.899	0.901	0.904	0.909	0.910	0.911	0.915	0.928	0.936
172.	*****	*****	*****	*****	0.909	0.900	0.896	0.896	0.899	0.903	0.905	0.907	0.911	0.922	0.931
173.	*****	*****	*****	*****	0.914	0.905	0.898	0.895	0.896	0.901	0.902	0.907	0.909	0.925	0.924
174.	*****	*****	*****	*****	0.918	0.909	0.900	0.895	0.895	0.899	0.899	0.903	0.909	0.919	0.921
175.	*****	*****	*****	*****	0.919	0.915	0.902	0.898	0.897	0.900	0.900	0.905	0.906	0.917	0.922
176.	*****	*****	*****	*****	0.923	0.917	0.909	0.903	0.903	0.906	0.906	0.908	0.911	0.917	0.926
177.	*****	*****	*****	*****	0.924	0.919	0.916	0.910	0.908	0.909	0.910	0.912	0.916	0.921	0.921
178.	*****	*****	*****	*****	0.924	0.925	0.919	0.918	0.917	0.917	0.917	0.920	0.923	0.924	0.928
179.	*****	*****	*****	*****	0.923	0.920	0.919	0.919	0.919	0.923	0.922	0.923	0.929	0.928	0.936
180.	*****	*****	*****	*****	0.925	0.921	0.919	0.920	0.921	0.923	0.923	0.924	0.929	0.930	0.936

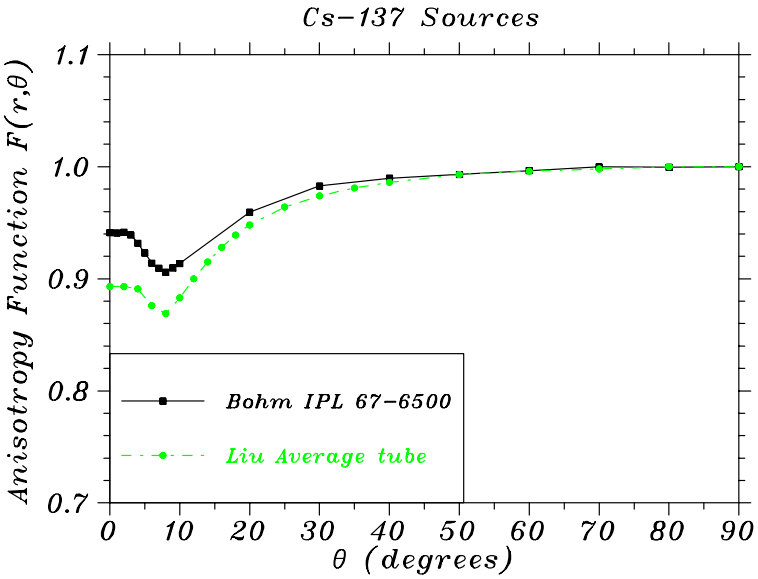

Figure 10: Anisotropy function profile at r=2cm for for IPL 67-6500 tube source versus Liu for *average* ^{137}Cs sources.

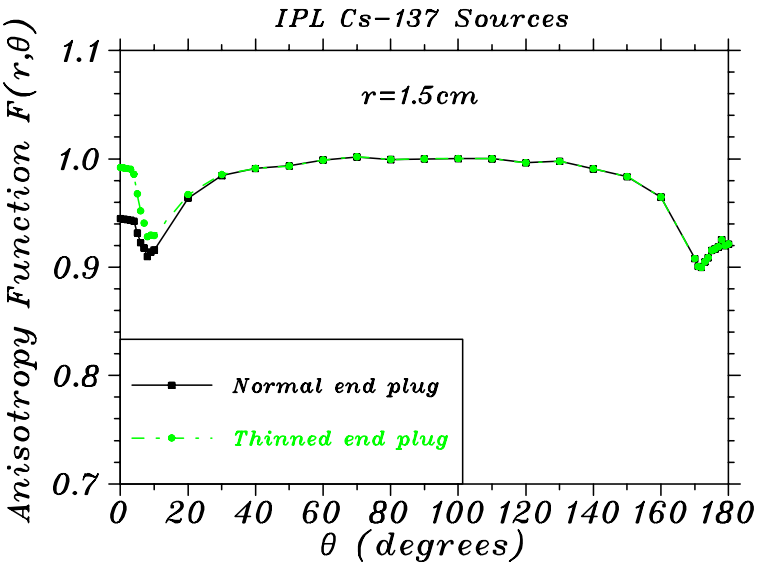

Figure 11: Anisotropy function profile at r=1.5cm for standard IPL 67-6500 tube source and a modified IPL tube source.

5 Air Kerma Strength S_K

Figure 12 shows a plot of the air kerma times source-detector distance squared versus distance from a source for the IPL tube source and a bare point ^{137}Cs source. The air kerma is scored in the transverse plane of the source using the ring version of the next event estimator and using energy absorption coefficients from Hubbell and Seltzer [10] with the source centered in a 700cm diameter sphere of air.

There are several interesting features to note in Figure 12. First, looking at the result for the bare point source, there is a slight decrease in the product of air kerma and distance squared as the distance increases. This is due to attenuation of the photons in air. Next, the values of air kerma times distance squared for the bare point source are about 2.5% higher than for the actual source. This is due to the source self-attenuation and shielding by the encapsulation materials. Finally, for the actual source, the air kerma does not follow a point source falloff of $1/r^2$ near the source. This is evidenced by the sharp rise in the product of air kerma and distance squared for source-detector distances less than 10 cm.

Typically, the air kerma strength of a source is provided by source calibration (using experimental methods); however, it may also be determined using transport calculations. To determine the air kerma strength, the data in Figure 12 beyond the non-$1/r^2$ behavior is fit to an equation such as $K_{air}\ d^2 = S_K\ e^{-\mu\ d}$ or $K_{air}\ d^2 = S_K + \beta\ d$ [14, 15]. The resultant air kerma strength is then referred to using the notation $(S_K)_{pt}$ to indicate that a detector subtending a small angle (in this case a point) was used to score the air kerma. For the air kerma calculations necessary to determine the air kerma strength, the statistical uncertainty averaged less than 0.1%.

Calculations of the air kerma were also scored using the energy absorption coefficients from MCNP's *mcplib04* cross section library. These values of the air kerma were in good agreement with those calculated using the energy absorption coefficients from Hubbell and Seltzer (on average 0.37% higher). Table 3 shows the air kerma strength determined with both of these calculations. From a theoretical transport perspective, the value of air kerma strength determined using the MCNP *mcplib04* heating numbers is the more appropriate

value to use. Palani Selvam *et al.* reported an air kerma strength of 2.920 $cGy\ cm^2/h\ mCi$ for the Amersham CDCS-J source. This is slightly higher than that of the IPL source which would be expected since the CDCS-J source has slightly thinner encapsulation. Note however that Palani Selvam *et al.* used a different Cs-137 decay spectrum so comparison is difficult.

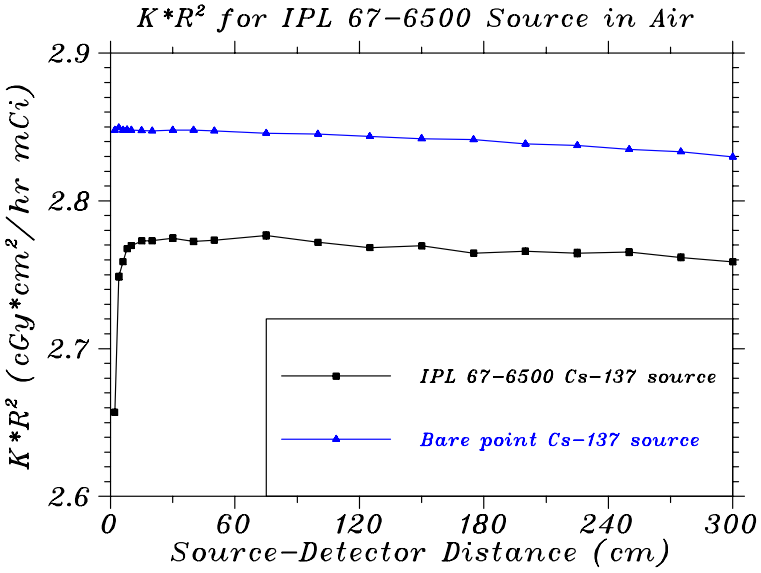

Figure 12: Air kerma times source-detector distance squared versus distance from a source for the IPL 67-6500 tube source and a bare point Cs-137 source. Note the activity units mCi refer to contained activity.

Table 3: Point detector based air kerma strength $(S_K)_{pt}$ for the IPL 67-6500 source. Note the activity units mCi refer to contained activity.

Energy Absorption Coefficients	$(S_K)_{pt}$ $(cGy\ cm^2/h\ mCi)$
Hubbell and Seltzer	2.7748
MCNP *mcplib04*	2.7851

Figure 13 shows a plot of the air kerma times source-detector distance squared as a function of polar angle (θ) at 30 cm distance from the IPL source. Note the reduction in air kerma at angles corresponding to the ends of the source. This is due to the end plugs and source self shielding. Near the transverse axis, the air kerma does not vary with polar angle.

Additionally, note that the air kerma is slightly lower at $\theta = 180^o$ (swage plug end) than the air kerma at $\theta = 0^o$. This is because the swage plug end has slightly thicker encapsulation materials in the source design. This difference in source output at the source ends is also evident in the anisotropy function.

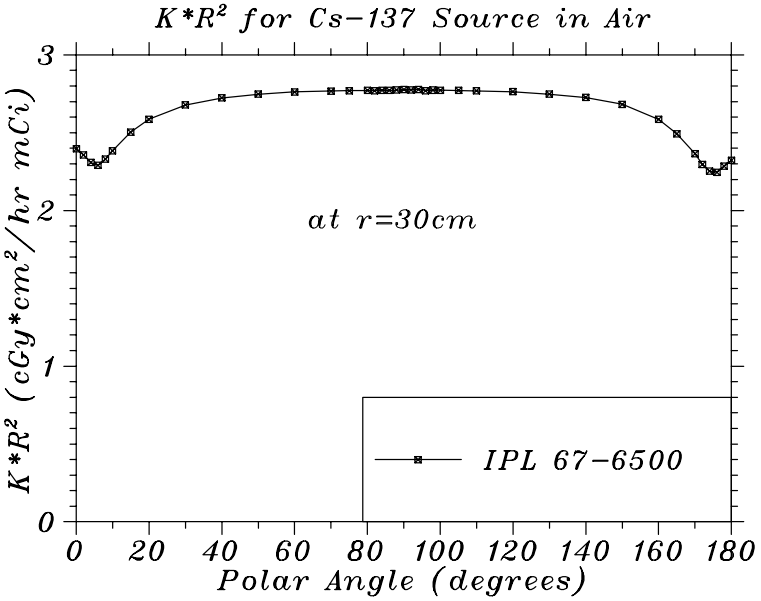

Figure 13: Air kerma times source-detector distance squared versus polar angle at r=30 cm for IPL 67-6500 tube source.

6 Dose Rate Constant Λ

Using the same depth dose data used to determine the radial dose function shown in Table 1 and the air kerma strength from Table 3, the dose rate constant was determined for the IPL source. Table 4 shows the dose rate constant determined using the energy absorption coefficients from MCNP's *mcplib04* cross section library and the energy absorption coefficients from Hubbell and Seltzer. Again, the *pt* subscript is used to indicate that a detector subtending a small angle (in this case a point) was used to determine the air kerma strength. From a theoretical transport perspective, the value of dose rate constant determined using the MCNP *mcplib04* heating numbers is the more appropriate value to use. Table 4 compares the dose rate constant obtained for the IPL tube source to the dose rate constants

published by other investigators for common tube sources. Agreement is generally good with the maximum difference of 2.74% seen in comparison to Williamson's published value for the Amersham CDCS-J source.

Table 4: Point detector based dose rate constant, Λ_{pt}, for the IPL 67-6500 source. Note that $1\,U = 1\ cGy\ cm^2/h$ =1 unit of air kerma strength.

Energy Absorption Coefficients	Λ_{pt} $(\frac{cGy}{h\,U})$
Hubbell and Seltzer	0.9556
MCNP *mcplib04*	0.9519

Table 5: Dose rate constants for a variety of Cs-137 tube sources. Note that $1\ U = 1\ cGy\ cm^2/h$ =1 unit of air kerma strength.

Author	Source Model	Λ $(\frac{cGy}{h\,U})$	Percent difference
Bohm	IPL 67-6500	0.9519	0
Casal [12]	Amersham CDCS-M	0.946	-0.62
Liu [13]	Amersham CDCS-J	0.977	+2.64
Liu [13]	RTR pre-1982	0.952	+.01
Liu [13]	RTR post-1982	0.948	-0.41
Liu [13]	3M 6500	0.968	+1.69
Williamson [11]	Amersham CDCS-J	0.978	+2.74
Williamson [11]	3M 6500	0.973	+2.22

References

[1] R. Nath, L.L. Anderson, G. Luxton, K.A. Weaver, J.F. Williamson, and A. S. Meigooni, "Dosimetry of interstitial brachytherapy sources: Recommendations of the AAPM Radiation Therapy Committee Task Group No. 43", Med. Phys. **22**, 209-234 (1995).

[2] M. J. Rivard, B. M. Coursey, L. A. DeWerd, W. F. Hanson, M. S. Huq, G. S. Ibbott, M. G. Mitch, R. Nath, and J. F. Williamson, "Update of AAPM Task Group No. 43 Report: A revised AAPM protocol for brachytherapy dose calculations", Med. Phys. **31**, 633-674 (2004).

[3] J. F. Briesmeister, Ed., "MCNP - A General Monte Carlo N-Particle Transport Code, Version 4C," Los Alamos National Laboratory report, LA-13709-M April, 2000.

[4] M. C. White, "Photoatomic data library MCPLIB04: A new photoatomic library based on data from ENDF/B-VI Release 8", Los Alamos National Laboratory Memorandom, LA-UR-03-1019, February, 2003.

[5] D.E. Cullen, J.H. Hubbell, L. Kissel, EPDL97: The Evaluated Photon Data Library, '97 Version, Lawrence Livermore National Laboratory report, UCRL-50400 Vol. 6, Rev. 5, September, 1997.

[6] J.A. Halbleib, R.P. Kensek, T.A. Mehlhorn, G.D. Valdez, S.M. Seltzer, M.J. Berger, *ITS Version 3.0: The integrated TIGER series of coupled electron/photon monte carlo transport codes*, Sandia National Laboratories report, SAND91-1634, March 1992.

[7] S. Y. F. Chu, L. P. Ekström, and R. B. Firestone, *WWW Table of Radioactive Isotopes*, database version 2/28/1999 online from URL http://nucleardata.nuclear.lu.se/nucleardata/toi/

[8] *Dosimetry of External Beta Rays for Radiation Protection*, International Commission on Radiation Units and Measurements, Report 56, Bethesda, MD, 1997.

[9] M. J. Berger, J. H. Hubbell, S. M. Seltzer, J. S. Coursey, and D. S. Zucker, "XCOM: Photon Cross Section Database (version 1.2)," [Online] http://physics.nist.gov/xcom National Institute of Standards and Technology, Gaithersburg, MD (1999). Originally published as M. J. Berger and J. H. Hubbell, "Photon Cross Sections on a Personal Computer," NBSIR 87-3597; and as M. J. Berger and J. H. Hubbell, "NIST X-ray and Gamma-ray Attenuation Coefficients and Cross Sections Database," NIST Standard

Reference Database 8, National Institute of Standards and Technology, Gaithersburg, MD (1987).

[10] J. H. Hubbell and S. M. Seltzer, "Tables of X-Ray Mass Attenuation Coefficients and Mass Energy-Absorption Coefficients (version 1.03)," [Online]. http://physics.nist.gov/xaamdi. National Institute of Standards and Technology, Gaithersburg, MD (1997). Originally published as NISTIR 5632, National Institute of Standards and Technology, Gaithersburg, MD (1995).

[11] J. F. Williamson, "Monte Carlo-based dose-rate tables for the Amersham CDCSJ and 3M Model 6500 ^{137}Cs tubes", Int. J. Radiation Oncology Biol. Phys., **41**, 959-970 (1998).

[12] E. Casal, F. Ballester, J. L. Lluch, J. Perez-Calatayud, and F. Lliso, "Monte Carlo calculations of dose rate distributions around the Amersham CDCS-M-Type ^{137}Cs source", Med. Phys. **27**, 132-140 (2000).

[13] L. Liu, S. C. Prasad, and D. A. Bassano, "Determination of 137Cs dosimetry parameters according to the AAPM TG-43 formalism", Med. Phys. **31**, 477-483 (2004).

[14] J. I. Monroe and J. F. Williamson, "Monte Carlo-aided dosimetry of the Theragenics TheraSeed (R) Model 200 Pd-103 interstitial brachytherapy seed", Med. Phys. **29**, 609-621 (2002).

[15] J. F Williamson, Z. Li, "Monte-Carlo aided dosimetry of the microselectron pulsed and high-dose-rate Ir-192 sources", Med. Phys. **22**, 809-819 (1995).

[16] T. Palani Selvam, K. N. Govinda Rajan, P. S. Nagarajan, B. C. Bhatt and P. Sethulakshmi, "Room scatter studies in the air kerma strength standardization of the Amersham CDCS-J-type 137Cs source: a Monte Carlo study", Phys. Med. Biol. **47**, N113-N119, (2002).

[17] X-5 Monte Carlo Team, "MCNP - A General Monte Carlo N-Particle Transport Code, Version 5," Los Alamos National Laboratory report, LA-UR-03-1987 April 24, 2003.